Alkali metal insertion in hard carbon – the full picture[†]

Holger Euchner,[*a] Bhaghavathi P. Vinayan,[*a] M. Anji Reddy, [b] Maximilian Fichtner, [a,c] and Axel Groß[a,d]

Carbon-based anodes are technologically highly relevant for Li and post–Li ion batteries. While the storage mechanism of Li in graphite is essentially understood, the alkali metal intercalation in carbon derivatives has been strongly debated. Here, we present a combined computational and experimental study on the intercalation of Li and Na in hard carbon, elaborating on the impact of the different alkali metals on the storage mechanism. Our results give strong evidence that the intercalation of Li and Na in hard carbon follow the same route and, moreover, show that in operando Raman scattering is a sensitive and powerful tool for characterizing the intercalation mechanism in carbon based materials. In fact, by exploiting the so–called double resonance, even information on the electronic structure can be obtained. Finally, theoretical predictions for the insertion mechanism of K are presented.

1 Introduction

Sodium and potassium ion batteries (NIBs and KIBs) are so-called post–Li systems that are in many ways complementary to the state-of-the-art lithium–ion batteries (LIBs). Especially the high abundance of sodium and potassium make these elements to attractive alternatives to lithium-ion technology. However, a key issue that has to be solved to successfully apply these post–Li systems in battery technology, is the development of suitable anode materials. While lithium is typically used with graphitic anodes, reaching a maximum Li–content corresponding to a LiC_6 stoichiometry, only tiny fractions of sodium can be intercalated into graphite, which is due to the fact that Na bulk metal formation and thus Na metal plating becomes thermodynamically more stable than additional Na intercalation into graphite[1]. This issue has fueled research in different carbon derivatives, in particular hard carbon, which has emerged as standard anode material in NIBs, yielding capacities of up to 300 mA h g^{-1}[2,3]. Interestingly, hard carbon is typically obtained from renewable bio-sources, such that the production is indeed cheap and sustainable. Potassium

on the other hand is able to intercalate into graphite up to KC_8 stoichiometry. Thus, graphite is in principle a suitable anode material for KIBs, however, still offering lower capacity than in the case of Li. Furthermore, it is interesting to note that graphite can be used as anode materials for Li and K, but not for Na. Hence there does not seem to be any systematic trend among the alkali metals.

Generally, the alkali metal insertion mechanism in non–graphitizable hard carbon, although still debated, is assumed to be different from the well-established stage intercalation of Li in graphite. Stevens and Dahn originally proposed the so–called card house model[2,3], which assumes that alkali metal ions are inserted between nearly parallel layers of carbon in the sloping potential region of the charge-discharge curve, followed by their adsorption in nanopores at the potential plateau. The alkali metal ions that are adsorbed in the nanopores were predicted to have metallic character, due the adsorption potential being close to metal deposition. In the case of sodium, this was confirmed by in operando ssNMR measurements, showing sodium to have a quasi-metallic character[4], which consequently was interpreted as a strong indicator for the adsorption in nanopores. Moreover, similar findings were obtained by ex situ Li NMR measurements on lithiated hard carbon[5]. An investigation of sodium storage in different types of hard carbons with distinct defect concentrations was correlated to the slope of the charge–discharge curve, showing an increasing slope for higher defect concentrations[6]. Similar results were obtained from first principle studies of Na intercala-

[a] Helmholtz Institute for Electrochemical Energy Storage Ulm, D–89081 Ulm, Germany

[b] Future Manufacturing Research Institute, College of Engineering, Swansea University, Swansea SA1 8EN, United Kingdom

[c] Institute of Nanotechnology, Karlsruhe Institute of Technology, D–76021 Karlsruhe, Germany

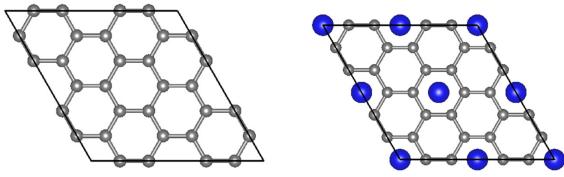[d] Institute of Theoretical Chemistry, Ulm University, D–89081 Ulm, Germany

Fig. 1 Empty (AA-stacking of graphitic planes) and completely filled graphitic layers (AMC_6 stoichiometry), corresponding to charged and discharged compounds, respectively.

Fig. 2 Schematic description of a double resonance process, with respect to the electronic band structure in vicinity of the high–symmetry points $\vec{K}$ and $\vec{K}'$.

tion in bi–layer graphene, where the slopy part of the discharge was then assigned to the Na adsorption on defect sites[7]. Recently, the intercalation dependence on density and defect concentration in disordered carbon model structures was computationally investigated (for Li, Na, K)[8]. This study gives strong evidence for a card house like mechanism, yet, also indicates the importance of the exact microstructure of the utilized hard carbon. Finally, in a combined DFT and in operando Raman investigation, we were able to correlate the Na insertion in hard carbon with changes in the Raman signal, which can be understood in the context of an extended card house model[9].

Yet, there are studies proposing different mechanisms, which may partly originate from the complicated (and strongly preparation depended) structural morphology of hard carbon. Indeed, the application of standard bulk techniques such as X–ray diffraction seems difficult in the case of hard carbon. On the other hand, Raman spectroscopy has emerged as a highly sensitive technique for the characterization of carbon based materials. To further clarify the storage mechanism in hard carbon anodes, we present an in operando study of Li and Na intercalation in coconut shell derived hard carbon (CSHC) and interpret our findings by means of density functional theory (DFT). Finally, we extend our findings by a computational study towards the insertion of potassium.

1.1 Raman Scattering – the double resonance

In defect free graphite, the so–called G–band, typically appearing at ~ 1580 cm^{-1}, is one of the dominant Raman peaks and can be related to the in–plane motion of the carbon atoms in the graphene planes. Interestingly, in the presence of defects, additional intensity is observed at ~ 1360 cm^{-1} which is denoted as D–band. The D–band, however, does not stem from Γ–point phonons, but originates from a more complex inter–valley process, the so–called double resonance, which makes certain non–Γ–point vibrations accessible for Raman spectroscopy[11–13]. Such a double resonance Raman (DRR) process can be understood as a series of scattering events between an excited electron, a non–Γ–point phonon and a structural defect. First, an electron has to be excited to an empty state in the conduction band, meaning that the wave length of the Raman laser needs to match the energy difference between initial and excited electronic state. Then the excited electron interacts with the crystal lattice under creation (annhilation) of a phonon, before it is scattered at a lattice defect. Finally, the electron recombines with the hole it has created in the valence band and emits a photon with a reduced (increased) wave length, which is due to energy transfer to (from) the created (an-
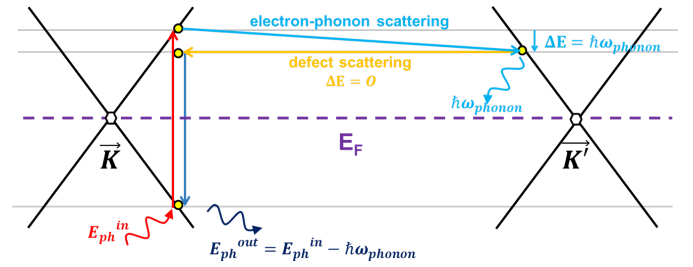
nihilated) phonon (see Fig. 2 for a schematic respresentation). Indeed, a DRR process has only a non–negligible probability if, close to high–symmetry points of the band structure, unoccupied states in the conduction band are accessible. For graphite, in the vicinity of the high–symmetry points $\vec{K}$ and $\vec{K}'$, these conditions are fulfilled. Here, the similarity of the graphite band structure to that one of graphene, which exhibits the famous Dirac cones precisely at these points of the Brillouin zone, should be noted.

To summarize, while first order Raman scattering in principle is a technique for the investigation of phonons in the vicinity of the Γ–point (i.e. wave vector q $\approx$ 0), DRR processes allow probing phonons far away from the center of the Brillouin zone. Consequently, DRR phenomena give access to additional information beyond standard Raman processes.

2 Results

2.1 In operando Raman

For the investigation of the Li and Na insertion mechanism in CSHC, in operando Raman measurements were conducted, giving access to Raman spectra and the corresponding charge/discharge curves (for details see Methods section).

In the case of Li–intercalation in the hard carbon, we observe a steep decrease of the voltage between the OCV and ~ 1.0 V (see Fig. 3a, right panel). At ~ 1.0 V the slopy part of the discharge curve starts, reaching down to ~ 0.1 V and comprising a capacity of ~ 180 mAh g^{-1}. Then, a large low voltage plateau is visible that extends up to a maximal capacity of 750 mAh g^{-1} in the first cycle. The reversible capacity can be estimated to ~ 600 mAh g^{-1} after the second cycle. Now, we have to connect the in operando Raman data in the left panel of Fig. 3a with the just discussed discharge curve. Indeed, in the slopy part of the discharge curve a downshift of the G–band (from 1600 cm^{-1} at OCV) is observed, reaching its minimum value of 1527 cm^{-1} at ~ 0.1 V. In the plateau region the G–band then remains essentially constant at this minimum value. For better readability, the evolution of the G–band frequency is also superimposed on the charge/discharge curve in the right panel of Fig. 3a. Moreover, the observed Raman spectra allow us to follow the evolution of the D–band. Indeed, the D–band remains centered at a frequency of 1327 cm^{-1} and only shows a variation in intensity, finally disappearing at a potential of ~ 0.17 V, i.e., still in the slopy region of the potential.

Before we continue and discuss the case of Na, it should be

noted that in situ studies of Li intercalation in graphite show a somewhat different behaviour for the G–band as compared to what is observed in hard carbon. For Li intercalation in graphite, only in the low potential region (below 0.3 V) a shift of the G–band towards lower frequency is observed. At higher potentials a splitting of the G–band is observed, which is a consequence of the distinct intercalation stages[14]. For hard carbon on the other hand, the G–band is a broad peak, which should rather be understood as representing an average over many different local environments.

Moving towards Na–intercalation, we find the overall picture to be very similar, which is in perfect agreement with our previous study[9]. First, the discharge profile shows a steep decrease down to 1.0 V, followed by the sloping region that extends to a capacity of about 90 mAh g^{-1} (see Fig. 3b, right panel). Then, as in the case of Li, an extended low–voltage plateau region is observed which ends at the maximum capacity of 260 mAh g^{-1}. Focusing on the Raman spectra in the left panel of Fig. 3b, we realize that the G–band is also showing a distinct shift towards lower energies. Again, the G–band reaches its minimum of 1542 cm^{-1} at the end of the sloping potential and remains constant at this value for the whole plateau region. Thus, the G–band behaves analogous to the case of Li–intercalation, indicating that the G–band shift is directly connected to the slopy part of the potential curve, whereas it is again found to remain constant for the plateau region. This is best seen from the superimposition of the G–band on the charge/discharge curve (see Fig. 3b, right panel). Furthermore, for Na intercalation the D–band is also found to remain at the same frequency during discharge, again only varying in intensity. Indeed, in agreement with the observation for the Li intercalation, the D–band finally disappears within the slopy part of the discharge, now at a potential of 0.25 V.

Despite the significant differences in capacity – in both the slopy part and the plateau region – Li and Na behave alike. This makes us conclude that both the Li– and the Na–insertion process in CSHC show the same characteristics for the discharge curves as well as for the associated Raman spectra.

Most authors agree that the discharge capacity in the sloping region of the potential corresponds to sodium/lithium insertion in between the layers of the disordered carbon sheets, and possibly the formation of the solid electrolyte interphase (SEI) during the first discharge[2,3]. On the other hand, the discharge capacity in the plateau region has typically been assigned to alkali metal adsorption into nanopores. However, this picture of the storage mechanism – in particular in case of sodium – still has not been fully accepted. In the following, we will show that the Raman spectra indeed can only be understood on the basis of the card house model (with some extensions). In addition, we show that the Raman spectra provide extremely detailed information that can be used for a general quantification of the intercalation process in carbon derivatives.

2.2 Computational Results

2.2.1 Phonon dispersion curves

In order to describe the properties of the Li, Na and K intercalation in hard carbon from first principles, we have mimicked the bulk fraction of hard carbon in a periodic setup, consisting of a stacking of two C_{24} carbon layers on top of each other (see methods section). Different alkali metal (AM) contents have then been represented by AMC_6, AMC_{12}, AMC_{24} and AMC_{48} model structures. For these structures, phonon dispersion curves have been determined which should be compared with the experimental Raman data. It has to be noted that only Raman active Γ–point phonons are accessible by a normal Raman process, i.e. in the case of the alkali metal intercalation in graphite derivatives one of these Γ–point modes represents the above introduced G–band.

The fact that the G–band vibrations correspond to in plane motion of the carbon atoms results in the alkali metal atoms not being involved in this motion. On the other hand, the changes for different alkali metal contents (i.e. during charge/discharge) can be understood in terms of charge transfer. In a simplified picture it can be assumed that the alkali metal atoms transfer their charge to the graphitic planes, such that the alkali metal content has an impact on the force constants within these planes, apparently with significant changes only for high alkali metal contents (see ESI†for detailed discussion).

Furthermore, the differences observed for the different alkali metals, can be understood by realizing that the layer distance increases with the size of the intercalated ion which results in slightly changed charge transfer from Li to the carbon layers as compared to the case of Na or K (see ESI†for detailed discussion). Hence, the intralayer force constants of the C–C bonds are altered to a varying extent, affecting the vibrational frequencies of the corresponding phonon modes accordingly. Here, it should be noted that the G–band in alkali metal free carbon layers is essentially independent from the layer distance. Therefore, the G–band can indeed be understood as a measure of charge transfer and C–C bond strength and is thus directly related to the amount of intercalated alkali metal ions (see ESI†for detailed discussion).

Now we turn to a detailed discussion of the position of the G–band as derived from our calculations (indicated by orange circles in Fig. 4). As expected, we find for both Li and Na a downshift of the G–band with increasing metal content. While the experimental and computational results agree very nicely, it should be noted that the G–band shift is more pronounced in the calculation. Interestingly, for the same alkali metal content the dispersion curves of Li and Na compounds are very similar, indicating that the impact of the respective alkali metal on the dispersion is similar as well. In fact, only for the AMC_6 we see significant differences between the Na and the Li compound, which particularly manifest in the G–band position. As discussed above, this shift indeed can be related to the charge transfer from the metal atoms to the carbon matrix, which then results in a change of the C–C bond strength and consequently in a shift of the vibrational frequency. On a qualitative basis, we observe that the alkali metal intercalation in the layers of our model structures results in a downshift of the G–band frequency with increasing metal content. Conse-
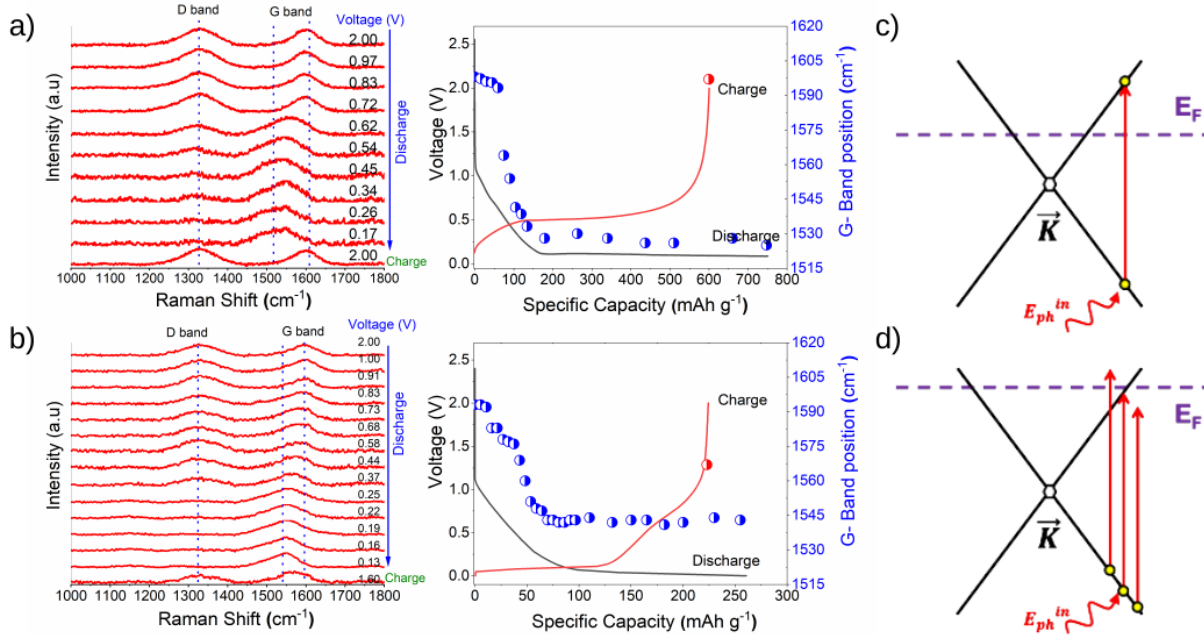
Fig. 3 a) In operando Raman spectra for Li insertion in hard carbon (left panel) along side with the corresponding charge/discharge curve and corresponding G–band position (right panel). b) Corresponding results for Na insertion (for additional spectra in the plateau region see ESI†). c) shows a schematic of the electronic band structure that allows for a DRR process and thus the occurrence of the D–band, while in d) the Fermi level is shifted such that no free states are available and thus no DRR process is possible.

quently, a shifting G–band can be understood as clear signature of the intercalation process. The absolute G–band shift can even be used as a general quantitative measure of the amount of intercalated ions. The different intercalation limits for Li and Na are then reflected by different minimum frequencies of the G–band, as is indeed observed in our experimental data shown Fig. 3a and b. Consequently, a constant G–band frequency, as observed for the plateau region, means that no further ions are intercalated, such that the capacity in this region can be assigned to the filling of the nanopores.

2.3 Electronic structure

As discussed in the introduction, the prerequisite for the occurrence of a DRR process and thus the D–band is the availability of empty states in the band structure, in the vicinity of the K–point above the Fermi level. To investigate our model compounds with respect to this feature, we have calculated the electronic band structure and again back–folded it to the first Brillouin zone of graphite (see also Methods for more details). The back–folded band structures of Li_xC_{48} and Na_xC_{48} are depicted in Fig. 5 and clearly show the impact of the alkali metal intercalation. Indeed, in a simplified picture, the alkali metal atoms donate their valence electrons to the electronic bands of graphite, thus resulting in a up–shift of the Fermi level, as depicted in the schematics in Fig. 3c and d. Hence, an increasing alkali metal content causes a continuous up–shifting of the Fermi level which ultimately results in a lack of available free states in the conduction band. Therefore, as a consequence of intercalation we expect a disappearing D–band in the Raman spectra at a certain alkali metal content, as is in-

deed observed experimentally. Detailed investigation of the band structure makes us realize that in case of lithium, empty states above the Fermi level are still accessible beyond LiC_{12}, while for sodium the accessible states are already shifted below the Fermi level for higher alkali metal contents. This means, for Li the DRR processes can still occur, whereas for Na they are no longer allowed. Thus, we conclude that in case of lithium intercalation, we should observe the disappearing D–band a bit later than in case of sodium, again in agreement with the experimental findings. Moreover, the potential at which the D–band disappears contains information on the electronic structure of the compound and thus the intercalation process: as long as the D–band is present there are still free states above the Fermi level which can be filled by alkali metal intercalation. Hence, the state of charge at which the D–band disappears may be interpreted as a lower bound for the intercalation limit. Moreover, it should be noted, that the observed constant position of the D–band also corresponds nicely to the fact that the phonon dispersion around the K–point in reciprocal space is not strongly altered. In Fig. 4 the black square indicates the rough position of phonon modes that are expected to contribute to the D–band intensity. Finally, we note that the back–folded band structures for lower Li/Na contents are qualitatively different. In the case of Li, we observe degenerate bands for the Dirac cone at the K–point for all Li contents, whereas in case of Na a splitting is observed for all cases except NaC_6. This splitting is again a consequence of the size of the intercalated ion and the increasing difference in layer spacing of empty and filled layers for Na as compared to Li (see ESI†for further discussion).
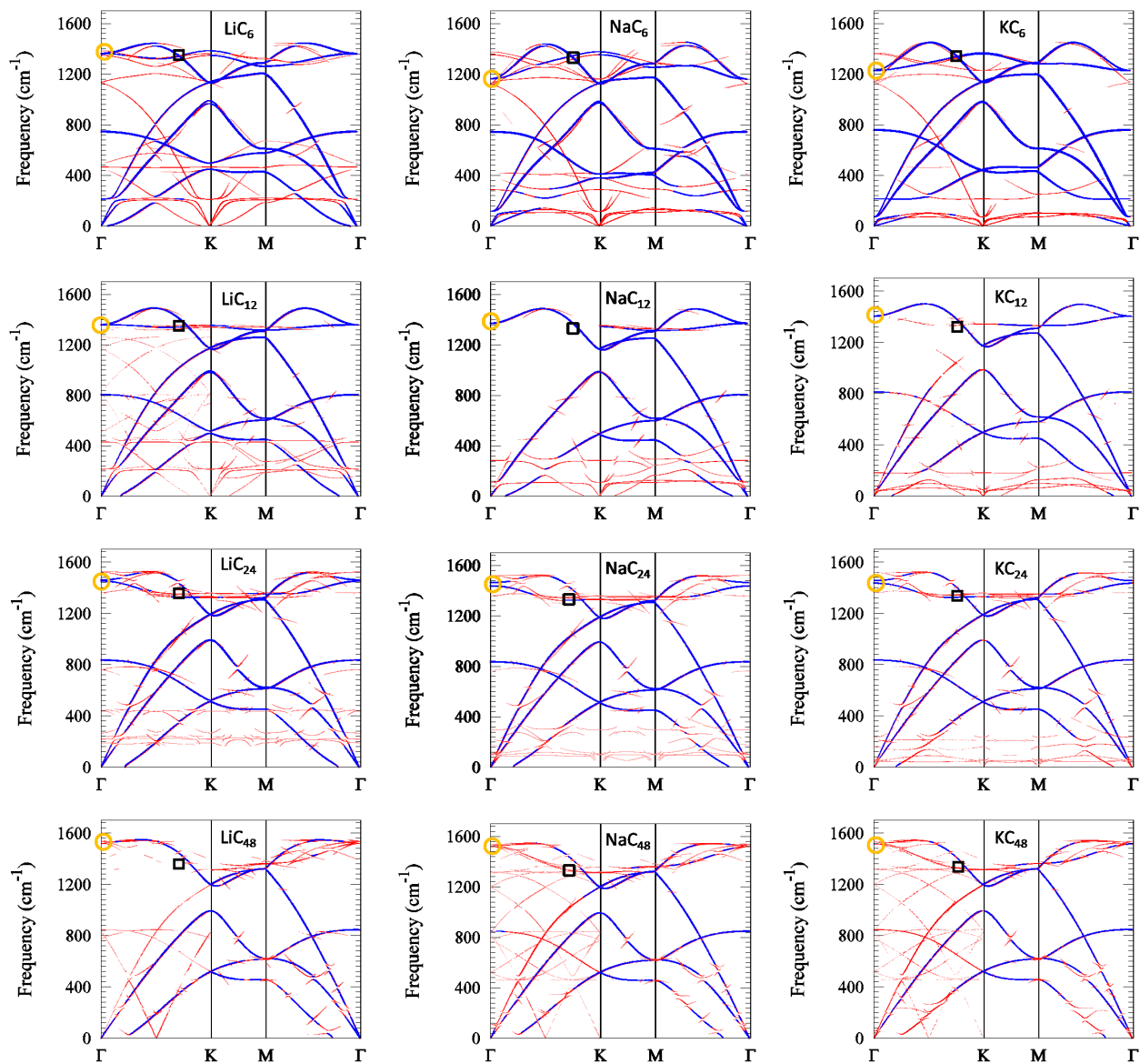
Fig. 4 Back–folded phonon dispersion curves for Li$_x$C$_{48}$ (left), Na$_x$C$_{48}$ (middle, see also ref. [9]) and K$_x$C$_{48}$ (right) as obtained from DFT. The position of the G–band and the estimated position of phonons that contribute to the D–band are indicated by orange circles and black squares, respectively.
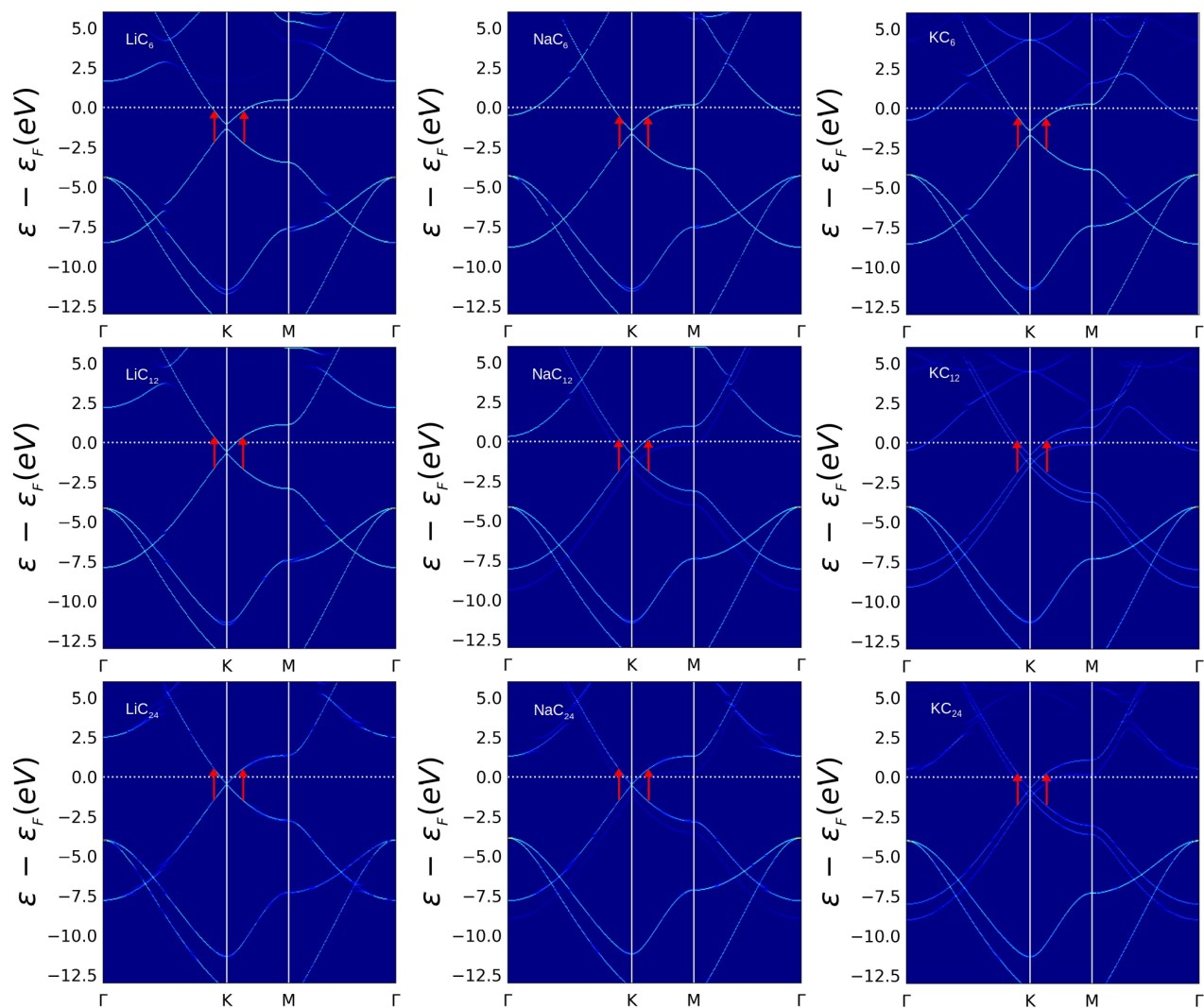
Fig. 5 Electronic band structure back–folded to the 1. Brillouin zone of graphite for Li_xC_{48} (left), Na_xC_{48} (middle, see also ref.[9]) and K_xC_{48}. The red arrows in the vicinity of the K–point in reciprocal space, correspond to the excitation energy of a laser with the experimentally applied wavelength of 633 nm ($\sim$1.96 eV).
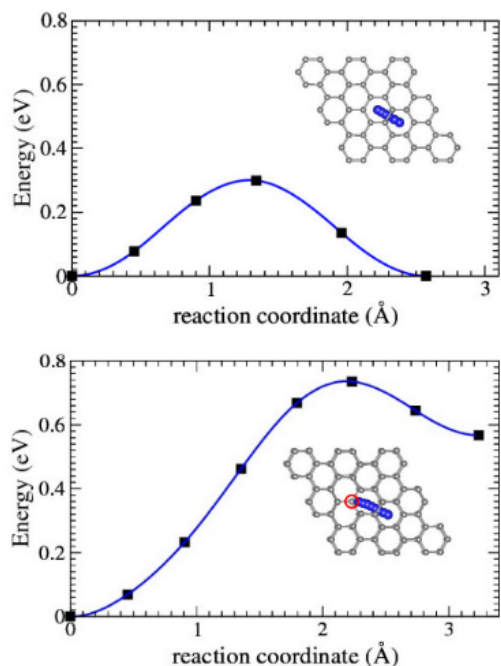
Fig. 6 Minimum energy path for Na diffusion in NaC_{48} and defect containing NaC_{47}, with the insets showing the NEB trajectories. The red circle indicates the position of the vacancy in the case of NaC_{47}.

2.3.1 Extension to the case of potassium

Our findings can now easily be extended to the case of potassium. For this purpose, we have calculated the phonon dispersion and electronic band structure for our model compounds with K_xC48 stoichiometry (see the right panels of Figs. 4 and 5). As expected, we find a behaviour again very similar to that of the Na and Li intercalation compounds. Here, it should be noted that both electronic and phonon band structure for K intercalation show only minor differences to the results for Na. This actually indicates that Na and K intercalation are very closely related, while in fact Li behaves slightly different. This is in good agreement with recent investigations that have identified Li and not Na as the outlier when comparing the bonding characteristics of alkali metal intercalation[15].

2.3.2 Pore filling

While our study is able to give direct insight in the intercalation process in the slopy part of the potential, the constat G–band position in the plateau region allows to assign it to the filling of the nanopores. However, in the flat potential region, the observed capacities correspond to significantly different amounts of stored Li and Na. Interestingly, for K intercalation in hard carbon an even smaller plateau region is observed than for Na[16]. A possible explanation was thought to lie in the diffusion properties of the alkali metal atoms. Hence, we have elaborated on the kinetics of the alkali metal diffusion in graphitic materials. For this purpose we have determined the corresponding diffusion barriers in the limit of low alkali metal concentration (high vacancy limit). Here, it is interesting to note, that we find the diffusion

barriers to scale inversely with the alkali metal masses and the corresponding ion sizes, as was also reported earlier for the low vacancy limit[17]. While we find a barrier of 0.4 eV in case of a diffusing Li atom, the barriers are reduced to 0.3 eV and 0.16 eV for Na and K. The diffusion pathways are examplified in Fig. 6 for the case of Na. In fact, the different barriers actually originate to a large extent in the different c–axis lattice parameters. This becomes obvious when the diffusion barriers for K diffusion in the graphitic model structure with the layer spacing of LiC_{48} are determined. For this scenario we obtain a barrier of 0.36 for K–diffusion (compared to 0.4 eV for Li). Conversely, Li diffusion for a layer spacing corresponding to KC_{48} is hindered by a barrier of 0.26 eV (as compared to 0.16 for K). Thus there is a significant impact of the layer spacing on the diffusion properties. Still, potassium diffusion barriers remain somewhat lower than those of Li and Na. This trend agrees well with recent DFT studies for alkali metal diffusion on graphene[18]. Furthermore, as already discussed earlier[9], the presence of vacancies indeed has a strong impact on the diffusion barriers (see Fig 6). The trend among the alkali metals, however, remains such that the barriers again are found to decrease from Li to Na to K. In fact, when defects are present, there is a significant static contribution to the diffusion barrier, originating from the difference between initial and final state. As expected, the alkali metals prefer to intercalate close to defects, such that the diffusion from a defect site to a non–defect site goes along with an additional energy penalty. Indeed, for Na we find 0.57 eV difference between initial and final state, while for Li we find 0.78 eV and 0.39 eV for K. This actually means, that the trapping of an alkali metal is more likely in the case of Li. Thus, if the processes were diffusion limited, we would actually rather expect higher capacities for K and Na.

Keeping in mind that the alkali metal species in the nano pores expose quasi–metallic character (see introduction), the different capacities might actually reflect the metal properties, rather than those of the hard carbon. For the agglomeration of alkali metal atoms with metallic character, the cohesive energy may be used as a descriptor. It is defined as the energy gain of forming bulk material from isolated atoms:

$$E_{coh} = E_{bulk} - E_{atom} \qquad (1)$$

with E_{coh} the cohesive energy, E_{bulk} and E_{atom} the total energy of the alkali metal bulk phase and an isolated alkali metal, respectively. Indeed, the cohesive energy becomes less negative from Li (-1.71 eV/at) to Na (-1.11 eV/at) to K (-0.84 eV/at), such that the tendency for aggregation is strongest for Li and one consequently may expect a higher capacity. Moreover, the significantly increasing lattice constant of the alkali metals, resulting in the density of atoms per volume being more than three times higher for bulk Li than for bulk K, indicates that more quasi–metallic Li should fit in a pore as compared to Na and K. Thus, the cohesive energy and in particular size arguments hold as simple explanation for the observed capacity differences between the respective alkali metals.

3 Conclusion

Using a combination of in operando Raman measurements and first–principles calculations we have demonstrated that Na and Li intercalation in hard carbon proceeds in a very similar way, in accordance with a modified card house model[9]. In particular, for both cases a shifting G–band could be identified with the intercalation process in the sloping potential region, whereas the constant G–band position in the potential plateau can be associated with the alkali metal adsorption in the nanopores. Furthermore, our study shows that in operando Raman spectroscopy is a highly sensitive tool to monitor intercalation in battery electrodes, which in case of carbon based materials is able to yield information beyond the vibrational excitations. Due the existence of a double resonance and the resulting D–band, it is even possible to gain insight in the impact of the intercalation process on the electronic structure. Moreover, our study provides evidence that in case of potassium the same mechanism is operative, which consequently will also be detectable by Raman investigation with respect to G– and D–band. Finally, we have also discussed the diffusion barriers in the high vacancy limit, confirming that the large and heavy K ions actually diffuse faster than Na and Li, which may make potassium an attractive candidate when fast kinetics are needed. Here, the alkali metal diffusion in hard carbon is important to grant fast access to the capacity in the nano pores. On the other hand, the faster kinetics of potassium is paid up with significantly lower capacity, in particular in the nano pores, which can be understood by differences in cohesive energy and atom size. Therefore, to improve the capacity of hard carbon anodes, in particular for sodium and potassium, the pore design is indeed crucial.

4 Methods

4.1 Computational

The computational investigations were conducted using the periodic density functional theory (DFT) code VASP[19,20], with the optPBE exchange–correlation functional[21], additionally accounting for van der Waals interactions via a non–local correction scheme[22]. The electron–ion interaction was described by the projector augmented wave (PAW) method[23].

All bulk model structures, are based on different degrees of filling of a $2 \times 2 \times 2$ supercell of the LiC_6 structure (see Fig. 1) and were optimized with respect to cell volume and atomic position. Note that the simulation cell corresponds to two C_{24} carbon layers on top of each other with periodicity also along the stacking direction, thus mimicking graphitic bulk fractions of hard carbon. In the case of Li intercalation it is well known that LiC_6 stoichiometry can be reached, whereas for Na only tiny fractions can be intercalated. However, the fraction of Na that can be intercalated, has been shown to increase significantly, when defects are considered[7,9]. While defects destroy the periodicity, thus complicating the calculation, it was shown that the main features of the electronic and phononic band structure are not significantly affected. Consequently, also in case of Na, we have only investigated defect–free model structures. The structural optimization was conducted for a $6 \times 6 \times 6$ k–point mesh and a cutoff energy of 600 eV. Phonon dispersion curves were obtained by using the phonopy code and the finite displacement method[24]. For this purpose the restoring forces for symmetry non–equivalent displacements were calculated by the VASP code, using the above described settings. To allow for a comparable representation, the phonon dispersion curves were back–folded on the high–symmetry directions (Γ–K—M–Γ) of reciprocal lattice of graphite. This was achieved by applying Phonon Unfolding code[25]. The electronic band structure was treated in a similar way, also applying a back–folding scheme with respect to high–symmetry directions in the reciprocal lattice of graphite, as provided within the BandUp code[26,27].

Finally, for the determination of diffusion barriers in the high vacancy limit the climbing image nudged elastic band method (NEB) was used[28,29]. For this purpose, the diffusion path of a single alkali metal atom was investigated in a defect–free C_{48} and a defective C_{47} structure.

4.2 Experimental

Coconut shell-derived hard carbon (CSHC) with a particle size from 1–10 μm was obtained from fiber–free coconut shells. These were first crushed to pieces of less than 5 mm size and then further ball–milled for 12h at 300 rpm. The resulting powder was carbonized for two hours at 600 °C followed by a two hours heating under Ar flow at 1000 °C with heating rate of 5 °C min−1.

Raman spectra were collected at room temperature in the spectral range 1000–1800 cm^1 by using an inVia^{TM} confocal Raman microscope (RENISHAW) with an excitation laser of 633 nm wavelength. To avoid sample over–heating, the nominal laser power was filtered down to ∼1 mW. The slit opening of the confocal system was fixed at 65 μm and centered at 1859 μm. For the collection of spectra, backscattering geometry with a 50 × magnification objective was applied (confocal micro–Raman mode). To increase the signal–to-noise ratio, each spectrum was averaged over 5 accumulations of 10 s each.

The probed sample spot was continuously focused during the experiment using an autofocus function. Analysis of the Raman data was conducted using the inVia WiRE 4.4 Software. Operando Raman measurements were conducted using an ECC-Opto-Std (EL-CELL GmbH) electrochemical cell connected with the Raman microscope. Thick slurry containing hard carbon (HC) and polyviniylidene fluoride (PVDF) binder in the weight ratio of 95:5 was deposited onto a stainless steel (SS) current collector (16 mm) with a 1 mm hole in the middle. Electrodes were dried for 12 h in an oven at a temperature of 120 °C. The in–situ cell was assembled using the HC coated current collectors as a positive electrode, lithium or sodium metal pressed onto another SS foil was used as an anode. For the lithium operando cell, a borosilicate glass fiber soaked (80 μL) with 1M $LiPF_6$ in ethylene carbonate/dimethyl carbonate was used. In the case of the sodium operando cell, the borosilicate glass fiber was soaked (80 μL) with 1.0 M $NaClO_4$ in propylene carbonate (PC). The cathode side of the cell was sealed with a thin optical glass window (0.15 mm) and made air–tight with a rubber seal. The battery tester was an Interface 1000TM Potentiostat/Galvanostat/ZRA (Gamry Instruments, Inc.) electrochemical workstation with Gamry Echem

Analyst software.

The operando Raman cell for Na was discharged and charged between 2.5–0.002 V vs. Na/Na+ at a constant current density of 16 mA g^{-1}. The operando Raman cell for Li was discharged and charged between 2.5–0.002 V vs. Li/Li+ at a constant current density of 30 mA g^{-1}. Finally, it should be noted that the capacity that is obtained from the operando Raman measurement may be influenced by cell geometry, mass loading of the electrode material, and applied current density.

Conflicts of interest

There are no conflicts to declare.

Acknowledgement

Notes and references

1 Z. Wang, S. M. Serbach and T. Grande. Van der Waals density functional study of the energetics of alkali metal intercalation in graphite. *RSC Advances*, 8(4):4069–4079, 2014.

2 D. A. Stevens and J. R. Dahn. High Capacity Anode Materials for Rechargeable Sodium-Ion Batteries. *Journal of The Electrochemical Society*, 147(4):1271, 2000.

3 D. A. Stevens and J. R. Dahn. The Mechanisms of Lithium and Sodium Insertion in Carbon Materials. *Journal of The Electrochemical Society*, 148(8):A803, 2001.

4 Joshua M. Stratford, Phoebe K. Allan, Oliver Pecher, Philip A. Chater, and Clare P. Grey. Mechanistic insights into sodium storage in hard carbon anodes using local structure probes. *Chemical Communications*, 52(84):12430–12433, 2016.

5 K Guérin, M Ménétrier, A Février-Bouvier, S Flandrois, B Simon, and P Biensan. A 7Li NMR study of a hard carbon for lithium–ion rechargeable batteries. *Solid State Ionics*, 127(3-4):187–198, 2000.

6 Zhifei Li, Clement Bommier, Zhi Sen Chong, Zelang Jian, Todd Wesley Surta, Xingfeng Wang, Zhenyu Xing, Joerg C. Neuefeind, William F. Stickle, Michelle Dolgos, P. Alex Greaney, and Xiulei Ji. Mechanism of Na-Ion Storage in Hard Carbon Anodes Revealed by Heteroatom Doping. *Advanced Energy Materials*, 7(18):1602894, 2017.

7 Ping-chun Tsai, Sai-Cheong Chung, Shih-kang Lin, and Atsuo Yamada. Ab initio study of sodium intercalation into disordered carbon. *Journal of Materials Chemistry A*, 3(18):9763–9768, 2015.

8 Jian-Xing Huang, Gábor Csányi, Jin-Bao Zhao, Jun Cheng, and Volker L. Deringer. First-principles study of alkali-metal intercalation in disordered carbon anode materials. *Journal of Materials Chemistry A*, 7(32):19070–19080, 2019.

9 M. Anji Reddy, M. Helen, Axel Groß, Maximilian Fichtner, and Holger Euchner. Insight into Sodium Insertion and the Storage Mechanism in Hard Carbon. *ACS Energy Letters*, 3(12):2851–2857, 2018.

10 F. Tuinstra and J. L. Koenig. Raman Spectrum of Graphite. *The Journal of Chemical Physics*, 53(3):1126–1130, 1970.

11 A. V. American Institute of Physics., A. N. Optical Society of America., Ya. S. Bobovich, V. I. Petrov, A. V. Baranov, A. N. Bekhterev, Ya. S. Bobovich, and V. I. Petrov. *Optics and spectroscopy.*, volume 62. [American Institute of Physics], 1987.

12 C. Thomsen and S. Reich. Double Resonant Raman Scattering in Graphite. *Physical Review Letters*, 85(24):5214–5217, 2000.

13 J. Maultzsch, S. Reich, and C. Thomsen. Double-resonant Raman scattering in graphite: Interference effects, selection rules, and phonon dispersion. *Physical Review B*, 70(15):155403, 2004.

14 Jianli Zou, Christopher Sole, Nicholas E. Drewett, Matěj Velický, and Laurence J. Hardwick. In Situ Study of Li Intercalation into Highly Crystalline Graphitic Flakes of Varying Thicknesses. *The Journal of Physical Chemistry Letters*, 7(21):4291–4296, 2016.

15 Yuanyue Liu, Boris V Merinov, and William A Goddard. Origin of low sodium capacity in graphite and generally weak substrate binding of Na and Mg among alkali and alkaline earth metals. *Proceedings of the National Academy of Sciences of the United States of America*, 113(14):3735–9, 2016.

16 Zelang Jian, Zhenyu Xing, Clement Bommier, Zhifei Li, and Xiulei Ji. Hard Carbon Microspheres: Potassium-Ion Anode Versus Sodium-Ion Anode. *Advanced Energy Materials*, 6(3):1501874, 2016.

17 Zhaohui Wang, Arne Petter Ratvik, Tor Grande, and Sverre M. Selbach. Diffusion of alkali metals in the first stage graphite intercalation compounds by vdW-DFT calculations. *RSC Advances*, 5(21):15985–15992, 2015.

18 Emilia Olsson, Guoliang Chai, Martin Dove, and Qiong Cai. Adsorption and migration of alkali metals (Li, Na, and K) on pristine and defective graphene surfaces. *Nanoscale*, 11(12):5274–5284, 2019.

19 G Kresse and J Furthmüller. Efficient iterative schemes for ab initio total-energy calculations using a plane-wave basis set. *Physical Review B*, 54(16):11169–11186, 1996.

20 G. Kresse and J. Furthmüller. Efficiency of ab-initio total energy calculations for metals and semiconductors using a plane-wave basis set. *Computational Materials Science*, 6(1):15–50, 1996.

21 Jiří Klimeš, David R Bowler, and Angelos Michaelides. Chemical accuracy for the van der Waals density functional. *Journal of Physics: Condensed Matter*, 22(2):022201, 2010.

22 M. Dion, H. Rydberg, E. Schröder, D. C. Langreth, and B. I. Lundqvist. Van der Waals Density Functional for General Geometries. *Physical Review Letters*, 92(24):246401, 2004.

23 G Kresse and D Joubert. From ultrasoft pseudopotentials to the projector augmented-wave method. *Physical Review B*, 59(3):1758–1775, 1999.

24 Atsushi Togo and Isao Tanaka. First principles phonon cal-

culations in materials science. *Scripta Materialia*, 108:1–5, 2015.

25 Fawei Zheng and Ping Zhang. Phonon Unfolding: A program for unfolding phonon dispersions of materials. *Computer Physics Communications*, 210:139–144, 2017.

26 Paulo V. C. Medeiros, Sven Stafström, and Jonas Björk. Effects of extrinsic and intrinsic perturbations on the electronic structure of graphene: Retaining an effective primitive cell band structure by band unfolding. *Physical Review B*, 89(4):041407, 2014.

27 Paulo V. C. Medeiros, Stepan S. Tsirkin, Sven Stafström, and Jonas Björk. Unfolding spinor wave functions and expectation values of general operators: Introducing the unfolding-density operator. *Physical Review B*, 91(4):041116, 2015.

28 Graeme Henkelman, Blas P. Uberuaga, and Hannes Jonsson. A climbing image nudged elastic band method for finding saddle points and minimum energy paths. *The Journal of Chemical Physics*, 113(22):9901, 2000.

29 H Jonsson, G. Mill and K. W. Jacobsne Nudged elastic band method for finding minimum energy paths of transitions. *Classical Quantum Dynamics in Condensed Phase Simulations*, ed. B. J. Berne, World Scientific, Singapore, 1998.